ADVANCED MATERIALS INTERFACES
www.advmatinterfaces.de

Voltage-Induced ON Switching of Magnetism in Ordered Arrays of Non-Ferrimagnetic Nanoporous Iron Oxide Microdisks

Matteo Cialone, Aliona Nicolenco, Shauna Robbennolt, Enric Menéndez, Gemma Rius, and Jordi Sort**

Tailoring the magnetic properties of ordered arrays of patterned structures usually requires stringent control of their size, pitch, microstructure, and composition. Here, a fundamentally different approach to manipulate the magnetic behavior of lithographed microdisks, based on the application of electrical voltage, is demonstrated. First, highly porous iron oxide films with virtually no magnetic response (OFF state) are grown by sol–gel chemistry. Subsequently, arrays of microdisks (8 μm in diameter) are obtained combining lithography with wet chemical etching processes. Electrolyte-gating (with an anhydrous electrolyte) is then employed to induce a tunable (i.e., "on-demand") ferromagnetic response in these disks (OFF–ON switching of magnetism) at room temperature. The changes in magnetic properties are attributed to magnetoelectrically-driven oxygen ion migration, which is enhanced due to nanoporosity. This causes partial reduction of the oxide phases to metallic Fe. The effect can be considerably reversed by applying voltage of opposite polarity. These results are appealing for diverse technological applications that require the use of patterned structures with easily tunable magnetic properties, such as magnetic micro-electro-mechanical systems, microfluidic, and lab-on-a-chip platforms for biomedical therapies and, ultimately, energy-efficient magnetic memories or neuromorphic computing.

1. Introduction

Over the years, patterned magnetic structures have found applications in a widespread range of technological areas. Micro-patterned magnetic films have been successfully integrated in a variety of micro-electro-mechanical systems such as magnetic sensors, actuators, or micromotors.[1,2] Arrays of magnetic micro-objects are being used in microfluidics, for droplet manipulation and particle trapping purposes.[3–5] Lab-on-a-chip platforms containing lithographed magnetic materials are utilized for single-cell positioning and confinement, as well as to guide cell growth and cell migration (i.e., micro-tissue engineering).[3,6–8] At the sub-micron length scale, periodic arrays of hard magnetic patterned dots have allowed a drastic increase of the areal density of information in hard disk drives.[9] In turn, arrays of soft magnetic nanodots have triggered the study of 2D artificial "spin ices"[10] and magnonic crystals,[11] amongst others. In most of these applications, device performance critically depends on fine tuning of the magnetic properties of the patterns. Parameters such as coercivity, saturation magnetization, remanence, or the magnetic easy axis direction need to be adjusted to meet specific technological demands.

To date, the fabrication of arrays of magnetic structures has mostly relied on conventional lithographic techniques in which the final properties depend on the interplay between the size/shape of the patterns and the composition of the motifs, in a unique and irreversible manner. Usually, the obtained properties cannot be further tailored once the fabrication process is finished. Only a few methods exist to tune the magnetic properties of materials after synthesis. Ion irradiation[12] and selective plastic deformation[13] have been used to induce structural disorder (atomic rearrangements) that cause irreversible changes in the magnetic behavior. The indirect coupling between spins and the electric or magnetic field components of light have been utilized to induce spin-reorientation, demagnetization, modification of the magnetic structure, or even magnetization reversal without need of directly applying magnetic fields.[14–16]

Dr. M. Cialone, Dr. A. Nicolenco, Dr. S. Robbennolt, Dr. E. Menéndez, Prof. J. Sort
Departament de Física
Universitat Autònoma de Barcelona
Bellaterra 08193, Spain
E-mail: Jordi.Sort@uab.cat
Dr. A. Nicolenco
Institute of Applied Physics
Chisinau 2028, Moldova
Dr. G. Rius
Institut de Microelectrònica de Barcelona
IMB-CNM (CSIC)
Bellaterra 08193, Spain
E-mail: Gemma.Rius@csic.es
Prof. J. Sort
Institució Catalana de Recerca i Estudis Avançats
Pg. Lluís Companys 23, Barcelona 08010, Spain
The ORCID identification number(s) for the author(s) of this article can be found under https://doi.org/10.1002/admi.202001143.

DOI: 10.1002/admi.202001143

Another interesting method to induce magnetization switching is to employ spin-polarized electric currents.[17] This is the operation principle of spin-transfer-torque random-access memories (STT-RAMs). Additionally, it has been suggested that reconfigurable magnetic metamaterials (composite materials with new functionalities emerging from combinations of nanoscale-engineered building blocks), suitable for magneto-plasmonic and magnonic crystal applications, can be prepared by scanning probe lithography.[18]

In parallel to the above-mentioned strategies, an alternative approach to control the magnetic properties of some materials in an energy-efficient manner is through the "converse magnetoelectric effect," that is, by the application of electrical voltage.[19–22] This method tackles the rather fundamental challenge of overheating that occurs in magnetic data storage systems due to the electric currents involved during the writing of magnetic information (resistive heating or Joule effect).[23] Electric field control of magnetism may allow for the implementation of ultralow-heat-dissipation memories operated at the nanoscale, involving energies around 10^{-18} J to write a bit,[24] much lower than the energy required to operate hard disk drives, STT-RAMs and other types of non-volatile memories.[25] In this case, voltage is applied through an insulating layer (virtually, with an infinite resistance) and, therefore, electron conductivity (leakage current flowing across the structure) is nearly zero, thereby minimizing the Joule heating effect.

Recently, magnetoelectric approaches have been realized in numerous classes of materials and architectures where an efficient modulation of various parameters, such as coercivity, magnetic moment, magnetic anisotropy, remanent magnetization, exchange bias, topological spin structures, etc. have been achieved.[19–22] Most of the research has been done on continuous films. However, reducing the lateral size of voltage-driven magnetic structures is essential to bring fundamental research in this topic to marketable devices. In addition, in arrays of dots, voltage might be easily applied, post-synthesis, to pre-selected motifs, eventually leading to a reconfigurable (reprogrammable) magnetic behavior. This method would be perfectly suited to tailor the magnetic properties of given patterns "on demand," varying the strength and polarity of the applied voltage, having potential for the development of voltage-controlled magnetic metamaterials or new concepts for data storage and processing (e.g., neuromorphic computing).[26] In the latter, voltage pulses could be used to trigger the onset of magnetism in synaptic circuits, similarly to ion channels in the brain.[26]

Among various magnetoelectric mechanisms that allow for voltage control of magnetism, magneto-ionics (i.e., electric-field-driven ion migration) has been recognized as one of the most scalable.[22] In certain semiconducting and dielectric materials, electric field induces ion migration of, for example, O^{2-},[27–29] Li^+,[30] H^+,[31] or N^{2-},[32] from the material of interest toward an ion reservoir or vice versa, depending on the voltage polarity. Diffusion of ions induces changes in the oxidation state of the metal, thus leading to large changes in magnetization. This procedure has been employed to tune the magnetic moment in a variety of materials.[19–22] In the extreme case, one can induce ON/OFF magnetic switching, that is, to generate (ON) or suppress (OFF) magnetism at will using voltage. Nevertheless, a full magnetoionic ON/OFF switching of magnetism has been accomplished only in a few systems, usually not at room temperature.[21] For instance, voltage-induced reversible modulation of magnetism has been achieved in ultra-thin Co films (<1 nm) adjacent to 2.5 μm-wide patterned bars of Gd_2O_3 as the gate oxide.[33] Applied electric field (−5 V) causes oxidation of ferromagnetic Co (ON) to antiferromagnetic CoO (OFF) as the oxygen ions are driven from the Gd_2O_3 reservoir toward the metal interface. Although the process is non-volatile and fully reversible, it requires the use of heat assistance (>470 K) to be triggered. Conversely, complex oxide heterostructures, such as perovskite $SrCoO_{3-\delta}$ actuated through an ionic liquid gate, require of low temperature (<225 K) to enable ON/OFF magnetic switching.[34]

Room-temperature ON/OFF switching of magnetization remains rather elusive. Specifically, this has been shown in electrolyte-gated Co_3O_4[29,35] and CoN[32] continuous (non-patterned) films in which voltage was used to change the oxidation state of cobalt, taking advantage of defect-assisted magneto-ionics. Likewise, room-temperature ON/OFF switching of magnetization has been realized via Li^+ intercalation/de-intercalation in α-Fe_2O_3 nanoparticles loaded onto a Cu foil cathode in a lithium ion battery.[30] Yet, α-Fe_2O_3 particles larger than 1 μm undergo irreversible changes in magnetism and cannot sustain large lithium intercalation.[30,36] Remarkably, almost complete ON/OFF switching was recently reported for β-FeOOH nanoplatelets in an alkaline Li-based electrolyte at room temperature[37] and electrodeposited Fe naturally covered by a thin layer of FeO_x tested in aqueous KOH solution.[38] However, in the former case, the platelet nanostructure collapsed after first voltage cycle and could not be recovered. In the latter case, a modulation of magnetization (up to 86%) was achieved by applying moderate voltages. Nonetheless, the presence of ferrimagnetic component in the starting FeO_x material precludes initial OFF magnetism. Also, in the aforementioned works, the particles/platelets are not arranged in a periodic (spatially ordered) manner, which makes it difficult to utilize the reported magneto-ionic effects in practical devices with targeted functionalities.

Iron oxides are earth-abundant, eco-friendly, biocompatible, and biodegradable materials, therefore being appealing candidates for magneto-ionic studies with a large potential to be employed in various technological fields. Yet, the structural versatility of FeO_x poses significant difficulties to synthesize the material in the desired phases or even to distinguish between phases in mixed iron oxide as-prepared systems. Often, as-deposited layers consist of a mixture of iron oxides with different Fe oxidation states and, thus, complex magnetic properties. Among the sixteen known iron oxides and oxyhydroxides, ferrimagnetic maghemite (γ-Fe_2O_3) and magnetite (Fe_3O_4), antiferromagnetic hematite (α-Fe_2O_3), paramagnetic wüstite (FeO),[39] and multiferroic luogufengite (ε-Fe_2O_3),[40] are the most commonly found in the literature. Importantly, iron oxides are widely utilized in areas such as energy storage, spintronic devices, or biomedical systems, thus having remarkable technological, economic, and societal impacts.[30,41,42]

From a microstructural viewpoint, magneto-ionic effects are typically enhanced in nanoporous structures as compared to archetypical dense films due to the increase of the surface-to-volume ratio. In metals, this allows for much larger accumulation of surface electric charge, since electric field is

screened at their outermost surface. In oxides, nanoporosity enhances both voltage-driven interfacial and volume-dependent magnetic effects, as the voids can accommodate various dielectric materials, such as high ion conductivity oxides or liquid dielectrics.[27,43] The size of the pore walls can be precisely controlled by adjusting the synthetic procedures, thus leading to interesting nano-in-micro miniaturized architectures.[44,45] Furthermore, nanoporosity brings a certain degree of mechanical flexibility to the films that is crucial for certain magnetically actuated systems.[46,47]

In this work, we investigate the use of magneto-ionics to trigger a voltage-driven OFF-ON switching of the magnetization in ordered arrays of nanoporous FeO_x microdisks. Nanoporous FeO_x layers are first fabricated by a non-aqueous sol–gel dip-coating method. Arrays of FeO_x nanoporous microdisks are then obtained by a top–down approach combining lithography and chemical etching processes. The initial magnetic state of FeO_x is tuned by controlling solution chemistry during the preparation of the sol–gel, and either ferrimagnetic or virtually non-ferrimagnetic states can be obtained from a single starting solution. Application of voltage to the non-ferrimagnetic (OFF state) nanoporous disks induces a considerable increase of the magnetic moment at saturation (ON state). The attainable value of saturation magnetization depends on the strength of the applied voltage. Furthermore, the induced effects can be considerably reversed by applying voltage of opposite polarity. The voltage-driven switching of magnetism is accompanied with structural phase transformations in FeO_x, including partial reduction to metallic Fe, caused by oxygen ion redistribution and ion exchange between the iron oxide and the liquid electrolyte. This work demonstrates a procedure to fabricate arrays of magnetic disks, where the properties can be adjusted "à la carte," after pattern fabrication, just by varying the strength of the applied voltage (i.e., in a fast, energy-efficient, and inexpensive manner). This is appealing for applications such as artificial neural networks, regenerative medicine, or metamaterials engineering, in which patterned magnetic structures with reconfigurable, on-demand magnetic properties are highly desirable.

2. Results and Discussion

Nanoporous FeO_x layers were grown onto Si/Pt substrates via dip-coating process (evaporation-induced self-assembly, EISA) from a non-aqueous ethanol sol–gel, as described in detail in the Experimental Section and illustrated in **Figure 1**a. Prior to

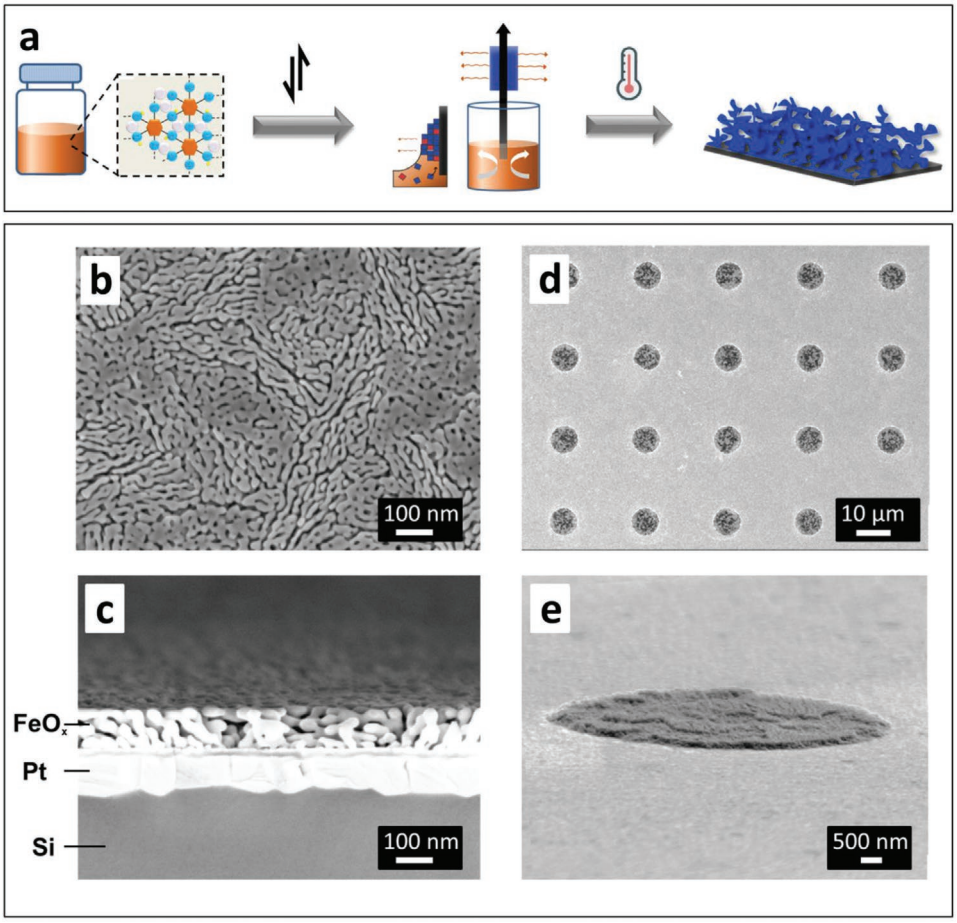

Figure 1. a) Schematic of the sol–gel synthesis of the FeO_x films. b) Top-view SEM image of the as-deposited FeO_x film. c) Cross-section image of the FeO_x film. d) An array of FeO_x microdisks obtained after wet chemical etching of continuous films. e) Tilted SEM micrograph of a single, nanoporous FeO_x microdisk.

deposition, the solution was allowed to age for different times, that is, 12, 24, 36, and 48 h, at room temperature. Deposited xerogels were annealed in air at 600 °C to crystallize the FeO_x phases. Figure 1b and Figure S1a, Supporting Information, show representative top-view scanning electron microscopy (SEM) images of the obtained nanoporous FeO_x films. The observed nanoporous structure originates from the solvent evaporation channels formed during the drying of the xerogels, which bring about 25% of porosity to the films. It is also worth mentioning that the degree of nanoporosity did not change significantly with the solution aging time and is primarily controlled by the solvent evaporation rate. SEM observations of a cross-section surface of FeO_x films (Figure 1c) demonstrate the development of a 3D nanoporous structure, with highly interconnected ligaments of 23 ± 6 nm in size, uniformly distributed across the whole thickness of the films (around 100 nm). The nanoporous character of the obtained films, together with the use of a liquid electrolyte (which is able to penetrate inside the pores), brings a drastic increase in the total area of "active" material that is affected by the electric field, thereby favoring an enhanced magnetoelectric response.[19,27,44] Simple geometrical estimations assuming, for example, a 100 nm thick film with 25% porosity comprising pores of 10 nm in diameter give an increase in the surface area by more than one order of magnitude (compared to a fully dense with the same thickness and lateral dimensions).

Subsequently, an array of nanoporous FeO_x microdisks was obtained from the films by combining optical photolithography with wet chemical etching procedures. Patterning of inherently nanoporous materials by wet etching is challenging due to the fast penetration of the etchant throughout the porous framework. In the case of 100 nm FeO_x films, it can result in partial or complete detachment of material from the substrate. Nevertheless, after optimization of the wet etching procedure, good pattern transfer was achieved, resulting in FeO_x microdisks with a well-defined circular shape (Figure 1d) and good integrity as shown in Figure 1e. Details on the thickness verification and the degree of nanoporosity after the etching are provided, respectively, in Figures S1b and S2, Supporting Information. No differences in the porosity degree or thickness with respect to the non-patterned films were observed. Furthermore, EDX elemental analysis confirmed that the composition of the films was preserved after patterning and that there are no residual iron compounds in between the microdisks (Figure S3, Supporting Information).

In the following, focus is first put on the evolution of the structural and magnetic properties of as-fabricated samples as a function of solution aging time. Next, samples with zero magnetization in the as-prepared state are selected in order to induce a variable magnetic moment post-synthesis, with the applied voltage. The effects of voltage on the phase percentages of the different oxides (and metallic Fe) in the disks, as well as the degree of reversibility of the process (with voltage of opposite polarity), are also investigated.

A remarkable aspect of this synthetic method is that despite the morphological similarities revealed for the FeO_x films deposited at various solution aging times, the resulting oxides exhibit distinct magnetic properties. **Figure 2** shows the dependence of the magnetic moment at saturation normalized to the films' lateral dimensions (M_S), in the as-prepared state,

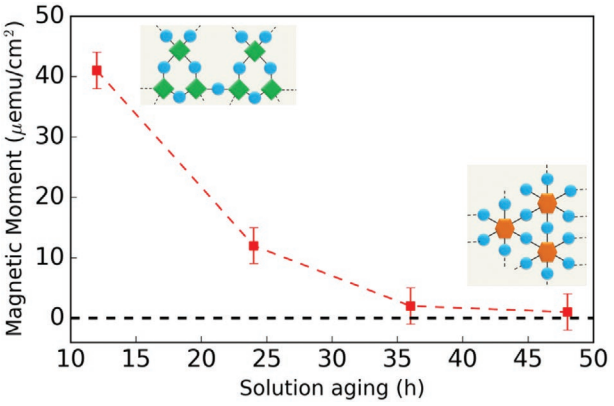

Figure 2. Magnetic moment at saturation normalized to the film's area of nanoporous FeO_x as a function of solution aging time. The magnetic moment of the films virtually vanishes, reaching an OFF state, after 48 h of aging of the solution. Insets show the schematics of Fe—O—Fe bonds formation during polymer network growth: green rhombus correspond to Fe^{+2} atoms, orange hexagons to Fe^{+3} and blue spheres correspond to oxygen- or hydroxyl-bridges.

as a function of solution aging time, measured by vibrating sample magnetometer (VSM) at room temperature. Note that given the nanoporous nature of the investigated oxides it is difficult to normalize the magnetic moment by volume. Hence, normalization was done per unit area (the thickness and lateral dimensions of all samples were kept constant in all the experiments, equal to 100 nm and 50 mm^2, respectively). Interestingly, the results show that the magnitude of M_S gradually decreases with an increase in sol–gel aging time. While the films deposited from 12 h solution exhibit a clear hysteretic behavior (presumably ferrimagnetic), the films produced from the 48 h aged solution are virtually non-ferrimagnetic, that is, they show an "OFF" magnetism in the as-prepared state (signal is below the threshold of detection).

So far, sol–gel has been widely used as a simple and cost-effective method to tune the magnetic properties of deposited iron oxides, but mainly in nanoparticles. However, despite the extensive literature dealing with the optimization of sol–gel synthetic procedures, the properties of the final material are still difficult to predict due to the complicated chemistry of the ongoing non-hydrolytic processes.[48] Sol–gel is accompanied by numerous complex chemical reactions involving formation of iron chelates and their condensation reactions with an organic O-donor (e.g., ethanol), which result in the formation of inorganic polymer chains containing oxygen- or hydroxyl-bridges.[49,50] In the case of iron oxides, the effect of aging is twofold: i) it promotes the growth of inorganic polymer chains that dictate steric constraints, that is, how the precursor species will be concentrated on the substrate by EISA during dip-coating and drying (Figure 1a), and ii) the metal precursor changes the oxidation state from Fe^{+2} to Fe^{+3}, which may be accompanied with a change in the coordination number of central metal atom and further branching of the polymers, as schematically illustrated in the insets of Figure 2. After the polymerization is complete and the excess of solvent is evaporated, the polymer precursors are oxidized, yielding a xerogel which after the heat treatment crystallizes into different oxide phases depending

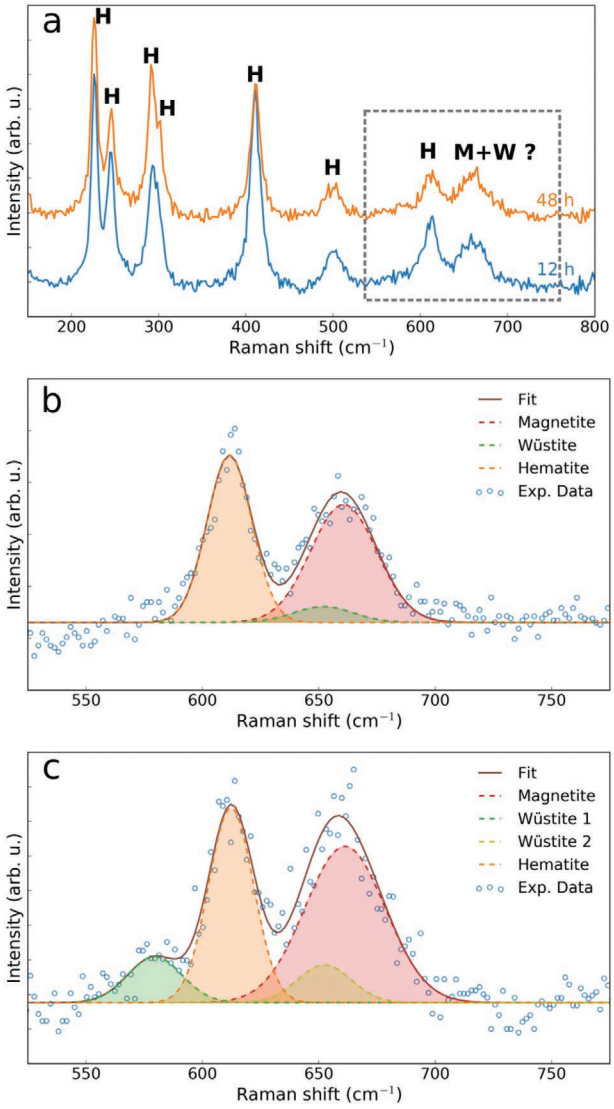

Figure 3. Raman spectra of as-prepared nanoporous FeO_x disks: a) Full spectra of the samples obtained after aging of the solution for 12 and 48 h. The following symbols are used: H—hematite, M—magnetite, W—wüstite. Fittings of the Raman peaks in the selected energy range (grey dashed rectangle) are shown in panel (b) and (c) for the 12 and 48 h samples, respectively. The results indicate a higher amount of wüstite present in the sample obtained after 48 h solution aging.

on its initial composition and microstructure. Accordingly, the microstructure of the xerogel is expected to have a direct influence on the magnetic properties of the FeO_x obtained after heat treatment. Previously, hematite (α-Fe_2O_3), goethite (α-FeOOH), lepidocrocite (γ-FeOOH), or iron hydroxide phase ($Fe(OH)_3$) were identified in the xerogel obtained from aqueous Fe^{3+} sol–gels.[51,52] Yet, the literature dealing with the non-aqueous iron xerogels remains rather scarce.

Here, the phase composition of FeO_x samples obtained after annealing of organometallic xerogels was investigated by Raman spectroscopy. **Figure 3**a shows the spectra collected on the FeO_x disks corresponding to the two extreme cases according to Figure 2, that is, after solution aging for 12 h (relatively high magnetic signal) and after aging for 48 h (non-ferrimagnetic oxide). Given the results from Figure 2, one would expect to find higher amounts of ferrimagnetic phases, such as magnetite or maghemite, in the sample after aging for 12 h than in the sample after solution aging for 48 h. Reference Raman bands of iron oxides are known and well-documented.[53,54] Hence, assignation of the different peaks to the possible oxide phases is relatively straightforward. Yet, one should bear in mind that Raman spectroscopy is a surface characterization technique (that is, it probes only a limited depth of the actual film thickness). Hence, the correlation between Raman results and the volumetric magnetic results should be taken qualitatively rather than quantitatively. The results show that both FeO_x samples are mainly composed of hematite (α-Fe_2O_3), which gives rise to the sharp peaks located at 226, 289, 293, 302, 412, 500, and 612 cm^{-1}.[53,54] Yet, the origin of the peak at around 660 cm^{-1}, which was observed in several of the sol–gel grown FeO_x samples, remains rather ambiguous. This peak is commonly considered as the main Raman magnetite (Fe_3O_4) peak, although it can be broadened due to the presence of wüstite (FeO) phase, which has a Raman band at around 652 cm^{-1}.[54]

Even though it is not possible to directly extract fully quantitative information from the presented Raman spectra, the experimental data were deconvoluted by weighed fitting of the existing peaks in the range from 500 to 800 cm^{-1} (Figure 3b,c), in order to qualitatively describe the apparent subtle structural differences between the two samples. Interestingly, magnetite phase is found in both samples, even though magnetite typically tends to transform to hematite during air-annealing at elevated temperatures.[55] In fact, the presence of magnetite in the 12 h sample is probably the sole factor that explains its ferrimagnetic behavior, since hematite is very weakly ferromagnetic at room temperature and the presence of maghemite cannot be evidenced from the obtained Raman spectra. In both cases (Figure 3b,c), the broadening around the magnetite peak can be related to the presence of a small fraction of wüstite phase. Wüstite is a non-stoichiometric iron oxide (precisely, $Fe_{1-x}O_x$) and it is paramagnetic at room temperature. In the ferrimagnetic FeO_x sample (12 h) the fraction of wüstite is almost negligible. Conversely, in the sample prepared by aging the solution during 48 h, an additional wüstite band at around 590 cm^{-1} can be clearly observed, which indicates that this film contains a larger fraction of this paramagnetic phase (Figure 3c).

From the VSM characterization, the magnetic moment after aging for 48 h is virtually zero (OFF state), although Raman spectra of this sample indicates presence of a small fraction of magnetite. However, it has been reported that easy oxidation of wüstite to magnetite by the incident laser light may take place during the Raman measurements in air (particularly for incident laser power in the range 0.7–7 mW),[54] thus giving rise to a single broad intense peak around 630–700 cm^{-1}.[56,57] This phenomenon would support that the actual amount of wüstite might be even initially larger in the 48 h sample (Figure 3c) and partial conversion from wüstite to magnetite might have occurred due to the incident laser. Another added difficulty for the interpretation of the obtained Raman spectra arises from the fact that hematite itself may show an extra peak at 660 cm^{-1} due to disorder effects in nanocrystals produced by sol–gel

synthesis.[56] In any case, in the sample obtained after aging for 48 h, the relative area of the magnetite peak with respect to the overall area of all the other peaks is only around 15% (and this percentage is likely overestimated due to the aforementioned reasons).

In order to better understand the magnetic behavior of the 48 h sample in its as-prepared state, we used superconducting quantum interference device (SQUID) to measure the temperature dependence of the magnetization, from 300 to 50 K, while applying a magnetic field of 1 kOe. The results, which are shown in Figure S4, Supporting Information, reveal that the sample is weakly ferromagnetic at room temperature (with a low magnetic signal, of the order of 8.3 μemu, close to the noise level of the VSM) and a drop of the magnetization is observed around 225 K. This is the typical behavior of hematite, which becomes antiferromagnetic below the so-called Morin transition temperature, T_M.[58] In bulk hematite, T_M is around 260 K, but its value is typically reduced for small crystallite sizes. Actually, the fact that the transition is not abrupt but spanning of a wide range of temperatures is an indication of the polycrystalline nature of the film, with a relatively wide distribution of the grain sizes (according to the work of Özdemir and Dunlop and the range of T_M, the grain sizes can be estimated to range between 30 and 100 nm).[59]

Next, the magnetoelectric properties of electrolyte gated FeO_x microdisks with an initial OFF state (48 h) were characterized by VSM while applying different voltages in situ using anhydrous propylene carbonate (PC) treated with metallic Na as dielectric.[19] The magnetoelectric properties of ferrimagnetic FeO_x continuous films, that is, non-patterned, were characterized elsewhere.[27] The samples were placed inside a home-made electrochemical cell aligned in between the poles of the VSM electromagnet. The magnetic hysteresis loops were recorded after applying a constant voltage for a fixed amount of time (1 h). The sample was kept exactly at the same position during magnetoelectric measurements, thus the variations of the magnetic moment upon the application of different voltages can be directly compared to each other.

Normalized hysteresis loops measured at different applied voltages on the 48 h solution aging sample are shown in **Figure 4**a. For the as-prepared state (ΔV = 0 V), no ferromagnetic signal is detected. Moreover, the signal is close to the noise baseline of the VSM (which is estimated to be ±5 μemu for our conditions), thus, the sample can be considered to be in an OFF magnetic state. Once a negative voltage (ΔV = −50 V) is applied, a clear ferromagnetic behavior emerges, that is, a well-defined hysteresis loop is observed (the as-measured raw data of this sample and the background are shown in Figure S5, Supporting Information). Therefore, negative voltage induces a clear OFF→ON magnetic transition. The magnetic moment at saturation reaches approximately 46 μemu cm^{-2} (see Figure 4b). Interestingly, when reversing the sign of the applied voltage (i.e., ΔV = +50 V), the value of the magnetic moment at saturation decreases considerably, by about 76%, reaching a minimum value of 11 μemu cm^{-2}. The coercivity (H_C) also changes upon the application of the voltage sequence, from H_C = 160 Oe at ΔV = −50 V, to H_C = 327 Oe at ΔV = +50 V.

The OFF–ON magnetic transition can be also observed applying ΔV = −10 V. In this case, the voltage-induced magnetic

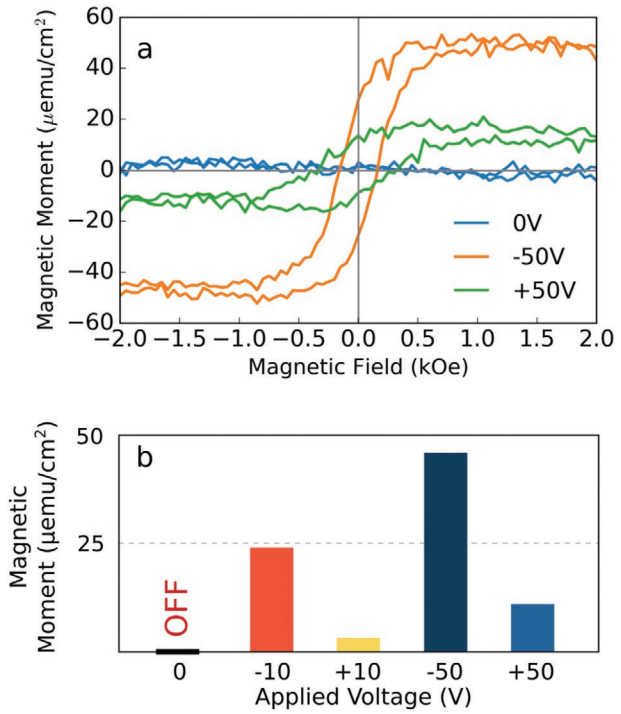

Figure 4. a) Room temperature hysteresis loops recorded along the in-plane direction while applying different voltages in situ on the sample prepared after 48 h solution aging. b) Absolute variation of the magnetic moment at saturation in the same sample while applying different voltage values.

moment at saturation is 24 μemu cm^{-2} and it reduces to 3 μemu cm^{-2} (noise level) after applying ΔV = +10 V (i.e., by a factor 87%). The changes in magnetic moment, which are compared in Figure 4b, reveal that from an initial OFF state, a set of different magnetization values (different ON states) can be subsequently obtained, on-demand, by simply subjecting the fabricated microdisks to applied voltage of variable strength.

To understand the physical changes and elucidate the mechanism that governs the OFF–ON transition, X-ray photoelectron spectroscopy (XPS) characterization was performed. XPS has the added value with respect to Raman that it is also sensitive to the presence of metallic phases, not only the oxides, and provides more accurate quantitative information. General surveys (Figure S6, Supporting Information) and high-resolution XPS spectra in selected regions of the sample were acquired at 0 V and after applying ΔV = −50 V and ΔV = +50 V (**Figure 5**). These voltages were selected since they are supposed to induce larger structural transformations than +/−10 V. Note that XPS measurements were acquired ex situ, after treating the sample in the electrochemical cell, whereas magnetic measurements were acquired in situ, during the application of the electric field. However, we verified that the magnetic state of the microdisks was stable for several hours (i.e., non-volatile) after removing the voltage. Therefore, it can be assumed that the acquired ex situ XPS spectra are still representative of the same state of the sample while it was measured in situ by VSM.

Figure 5 shows acquired spectra for the 48 h sample in its as-prepared OFF state (panel a), after applying ΔV = −50 V (panel b) and after applying ΔV = +50 V (panel c). The experimental data

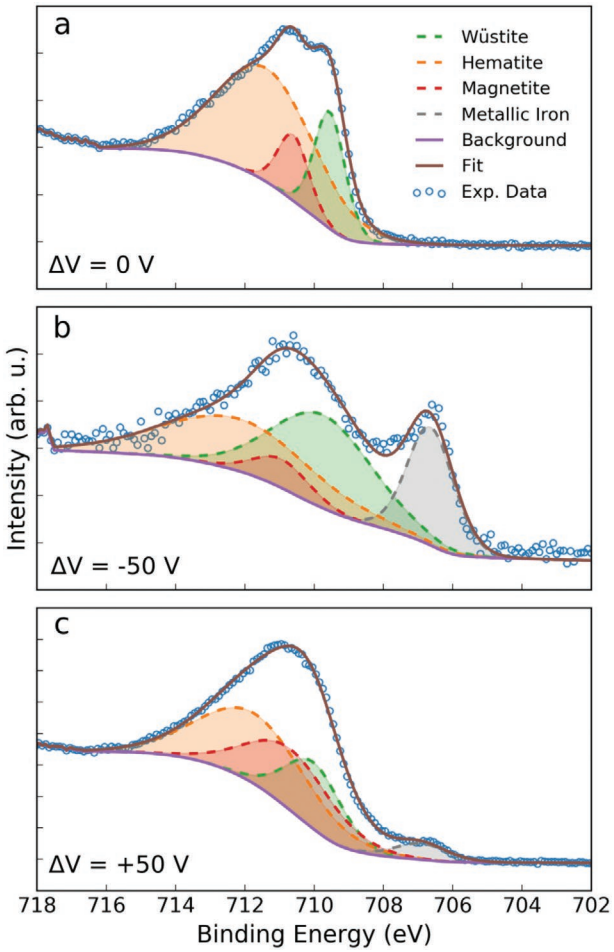

Figure 5. XPS spectra acquired on the sample prepared after 48 h solution aging, after applying a) $\Delta V = 0$ V, b) $\Delta V = -50$ V, and c) $\Delta V = +50$ V. The experimental data is shown together with a fit (using the CasaXPS software) and the deconvolution of the peaks from the different phases.

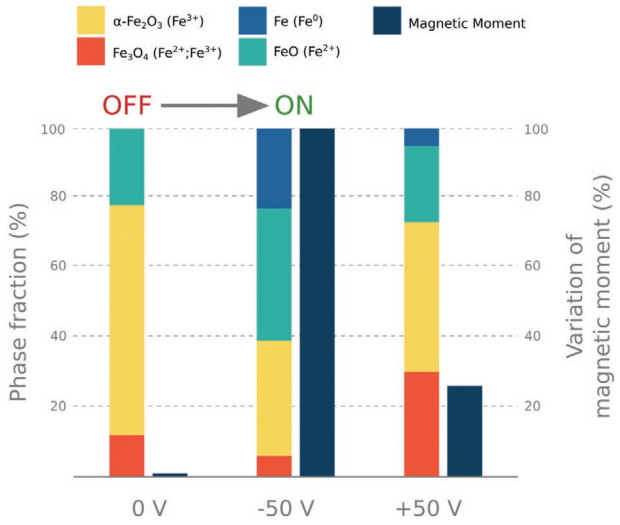

Figure 6. Summary of the XPS data and corresponding variation of the relative magnetic moment at saturation for the sample after solution aging for 48 h, at 0 V and after applying $\Delta V = -50$ V and +50 V. Phase percentages, determined from the relative area of the deconvoluted XPS peaks, are given in at.%.

are shown together with the deconvolution of the different components of plausible oxide phases and metallic Fe. The spectra were adjusted to the C—C peak, taking its position at the theoretical value 284.5 eV (using NIST X-ray Photoelectron Spectroscopy Database). Deconvolution of the $2p_{3/2}$ iron peaks was used to establish the relative amount of the different oxide phases present in the sample.[60,61] It should be noted that XPS is sensitive only to the outermost surface of the investigated material, in a depth range between 5–10 nm[62,63] due to the limited mean free path of the photoemitted electrons. Thus, strictly speaking, phase quantification by XPS corresponds to the outer surface of the samples.

The phase percentages obtained by XPS are summarized in **Figure 6** (and Table S1, Supporting Information). According to the fitting, in its OFF state, the sample comprises 22% of wüstite, 66% of hematite, and 12% of magnetite, while no metallic iron is detected. While applying $\Delta V = -50$ V, the sample undergoes a transition from OFF to ON magnetic states where ferromagnetism is clearly observable from the corresponding hysteresis loop (Figure 4a). XPS supports that this change in magnetic properties is the result of the changes in the phase composition. The most significant difference is the formation of metallic iron, which now represents a fraction of 23%. Simultaneously, the proportions of the other phases are also modified, with the magnetite content decreasing to 6%, hematite to 33%, and wüstite increasing to 38%. The presence of metallic iron is mainly responsible for the OFF→ON magnetic switching shown in Figure 4a, since the relative amount of magnetite decreases as compared to the as-prepared state. The amount of metallic iron reduces significantly after applying $\Delta V = +50$ V (down to 5%), while the fraction of iron oxides (particularly magnetite and hematite) increase significantly. This gives as a result a residual magnetic contribution after the positive voltage has been applied (Figure 4a).

As aforementioned, hematite and wüstite are weakly ferromagnetic and paramagnetic at room temperature, respectively, while magnetite is ferrimagnetic in the bulk. In fact, in magnetite, the Fe^{2+} and Fe^{3+} ions are typically found in a ratio of 1:2 and its ferrimagnetic behavior is given by the particular position of the Fe^{3+} and Fe^{2+} inside the crystal lattice.[64] At room temperature, the saturation magnetization for bulk magnetite is around 480 emu cm^{-3},[65] which is significantly lower than the saturation magnetization of metallic iron (1714 emu cm^{-3}).[66] Remarkably, the saturation magnetization in magnetite thin films can also be significantly reduced when the film contains excess oxygen (or iron vacancies). Values as low as 175 emu cm^{-3} have also been often reported.[65] Surface spin canting effects are also known to reduce the magnetization in low-dimensional materials (e.g., nanoparticles).[67]

Considering the results of the analysis of the XPS spectra, one could expect that a magnetite content of around 12% might manifest as a measurable (non-zero) magnetic moment in the as-prepared state. However, observing the hysteresis loop reported in Figure 4a, it is clear that the sample shows a null (i.e., not measurable by VSM) magnetic moment at 0 V (and, of course, no coercivity). As explained above, given the size of the

ligaments (pore walls) of the films (≈23 nm) it is indeed plausible that some surface spin canting effects occur, which would decrease M_S. Bearing in mind the measured value of magnetic moment at saturation after applying −50 V (46 μemu cm^{-2}), the ratio of saturation magnetization between pure Fe and bulk Fe_3O_4 (which is of the order of 1714/480 = 3.6), and the relative percentages of Fe and Fe_3O_4 in the −50 and 0 V samples, it is easy to calculate that the saturation magnetization of the sample in the as-prepared state would be around 6.2 μemu cm^{-2}, hence around the level of signal detection in the VSM. This is why the as-prepared microdisks (after solution aging for 48 h) exhibit a non-detectable magnetic signal by VSM in spite of containing 12% of magnetite. Finally, note that this 12% could be a bit overestimated since XPS only probes the outer surface of the films.

Concerning the coercivity, the value after applying +50 V is approximately twice the value obtained when the disks are first subject to −50 V. In a first approximation, this increase of H_C can be understood since in the sample subjected to negative voltage, all magnetic signal comes essentially from metallic Fe (which is soft ferromagnetic), whereas after applying +50 V, the measured magnetization originates both from metallic Fe and magnetite (semi-hard ferrimagnetic), which is now in larger amount than for the initial state at 0 V.

The phase transformations induced by application of negative voltages suggest a partial redistribution of oxygen atoms within the oxide phases, as indicated by an increased fraction of wüstite after −50 V was applied (see Figure 6; Table S1, Supporting Information). Furthermore, according to the oxide phase percentages calculated from the XPS data, the system loses about 25% of oxygen upon applying $\Delta V = -50$ V. This is consistent with a magneto-ionic mechanism based on oxygen ion migration. Under negative voltage O^{2-} ions migrate out of the iron oxide toward the electrolyte, where they become stabilized by the polar PC molecules and eventually form soluble ionic compounds with the traces of Na^+.[27] It is worth mentioning that no bubbling was observed in the utilized voltage window. This implies that the actual amount of released oxygen ions (by volume) is low compared to the volume of PC, that is, it is below the solubility limit. Reversing the sign of the potential, for example, applying $\Delta V = +50$ V for 1 h, the composition of the film can be changed again close to its original as-prepared state. However, from XPS data, about 6% of oxygen ions stored in the electrolyte cannot be re-incorporated during application of the positive voltage. This is likely to be due to the limited oxygen transport in PC.[68,69]

Finally, magnetoelectric experiments were performed while applying negative and positive voltage values several times, consecutively (cyclability). The results, included in the Supporting Information (Figure S7, Supporting Information), indicate that, with the present processing conditions, the endurance of the process is limited. The difficulty of re-incorporate the oxygen from the PC back into the film ultimately leads to a small part of the metallic iron which cannot be re-oxidized under positive voltages ("pseudo"-OFF magnetic state). A second-order effect which may negatively affect the cyclability and cannot be completely ruled out in the investigated system is the possible polymerization of PC on the surface of nanoporous materials under positive voltages.[45] Energy dispersive X-ray spectroscopy (EDX) observations of the surface of FeO_x microdisks suggested the appearance of organic deposits after a series of negative/positive voltages. Figure S1c,d, Supporting Information, depicts that both the arrangement of microdisks and their nanoporous structure are generally preserved after magneto-electric measurements. Nevertheless, the products of PC degradation can block the interior of the nanopores of FeO_x, hence giving a residual magnetic contribution and hampering larger magneto-electric effects.

3. Conclusions

In this work, the magnetoelectric response of FeO_x nanoporous microdisks has been studied. By using the EISA technique in combination with dip-coating and post-deposition thermal treatments, highly porous thin films of iron oxide have been produced. The porosity is homogeneous across the surface and thickness of the films, with a porosity degree of 25% and an average ligament's size of ≈23 nm. From the films, periodic arrays of nanoporous microdisks have been fabricated using optical lithography in combination with chemical etching. Remarkably, the disks preserve the same porosity characteristics and magnetic properties of the non-patterned film. The effect of the solution aging on the magnetic properties of the films has been investigated with the aim of obtaining arrays of microdisks with virtually no magnetic behavior. These non-ferrimagnetic disks have been subsequently electrolyte-gated and a clear ferromagnetic response, with tunable values of the magnetic moment at saturation, has been obtained. This has been possible due to the voltage-induced variation in the oxidation state of the iron atoms (including partial reduction to metallic Fe), as demonstrated by XPS. Reversing the voltage polarity leads to a considerable re-oxidation (reversed magneto-ionic effect). These results demonstrate that arrays of disks with targeted magnetic properties can be obtained "on demand" from an initially non-ferrimagnetic state, by simple application of voltage. In more complex structures, if voltage would be applied selectively to individual patterned dots or groups of dots, this would allow the fabrication of multi-component systems with new voltage-engineered functionalities (e.g., magnetic metamaterials). In turn, our results pave the way toward voltage-actuated magnetic data storage media, provided that the size of the patterned structures would be reduced toward the sub-20 nm length scale (to achieve sufficiently high recording densities).

4. Experimental Section

Preparation of Nanoporous FeO_x Layers and Arrays of Microdisks: A sol–gel was obtained by dissolving $FeCl_2{\cdot}4H_2O$ (400 mg) and citric acid (380 mg) in ethanol absolute (10 mL). The solution was stirred in a closed vial for 48 h at 500 rpm at room temperature and was never precipitated. The color of the solution changed with the aging time, starting from light green right after mixing the components, evolving to dark green after 12 h and becoming dark brown after 24 h, remaining stable until the final aging time of 48 h. Silicon chips metallized with a 70 nm thick sputtered Pt layer were used as substrates for FeO_x films deposition. The substrates were cleaned in nitrogen plasma and soaked in 0.4 M KOH solution (1:1 H_2O:C_2H_5OH mixed solvent) for 5 min to increase wettability of the surface. The solution was deposited by

dip-coating with a withdrawal rate of 300 mm min^{-1} using a Coater 5 AC from id Lab at room temperature and 50% relative humidity. The dip-coating procedure was applied for the solution stirred for 12, 24, 36, and 48 h. After dip-coating the samples were promptly transferred to a hot plate at 80 °C to assist fast solvent evaporation, yielding a nanoporous xerogel. To increase the thickness of the FeO_x layers the dipping process was repeated three times gently annealing the layers at 80 °C for 10 min after each cycle. As a final step, the samples were annealed at 600 °C for 3 h in air to crystalize the FeO_x oxide. A general scheme of the synthesis is shown in Figure 1a.

Ordered arrays of FeO_x microdisks were obtained by a top–down approach combining lithography and chemical etching processes. At first, arrays of resist cylinders were patterned onto the continuous nanoporous FeO_x layers by optical lithography, using photoresist AZ9260 and AZ400K developers. The patterned photoresist was used as a mask to protect FeO_x microdisks from etching. Wet chemical etching of FeO_x was performed in concentrated HCl acid (12 M) for 14 min. After the exposed part of FeO_x was etched away, the protective photoresist mask was removed by immersing the samples in dimethyl sulfoxide for 45 min, followed by a final gentle rinsing in acetone, isopropanol, and Milli-Q water.

Magnetic Characterization: In-situ room temperature magnetoelectric measurements were performed using a MicroSense (LOT-QuantumDesign) vibrating sample magnetometer (VSM), applying the magnetic field along the plane of the microdisks. The voltage was applied out-of-plane using an Agilent B2902A power supply through a home-made electrochemical cell attached to the VSM holder. An equivalent cell setup was reported elsewhere.[27] Briefly, the FeO_x sample acted as working electrode, and the electrical contact was made to the underlying Pt seed layer in a capacitor-like configuration.[35] A Pt wire was used as counter electrode. The two electrodes were placed parallel to each other in a small Eppendorf tube (1 mL) filled with propylene carbonate (PC) (anhydrous solution). Prior to magnetoelectric measurements, the electrolyte was externally treated with metallic Na to eliminate any traces of water. As a consequence, it contained a small fraction of Na^+ (≈5 ppm) and OH^- ions. No other salts were added. Voltage (negative or positive) was applied to the sample for 1 h and maintained during the hysteresis loops measurements, which took approximately 30 min. Apart from the FeO_x samples, magnetic hysteresis loops were also recorded for the spare Si/Pt substrate immersed in the electrochemical cell to serve as a reference baseline signal (Figure S5, Supporting Information). Subsequently, the substrate signal and all other contributions were subtracted from the magnetic hysteresis loops of FeO_x. To better understand the magnetic state of the as-prepared samples (after 48 h stirring), which does not show magnetic signal by VSM, low-temperature measurements were performed using a superconducting quantum interference device (SQUID), model Quantum Design MPMS-XL.

Morphology and Structural Characterization: The morphology of nanoporous FeO_x samples (in the as-deposited state and after voltage was applied) was observed by field emission scanning electron microscopy (FE-SEM) using a Zeiss MERLIN operated at 5 kV. Elemental analyses were performed by energy-dispersive X-ray spectroscopy (EDX) using the FE-SEM operated at 15 kV. The cross-section of FeO_x films was inspected by FE-SEM on cleaved samples. The degree of porosity and the ligament size were determined using the "ImageJ" image analysis software from the top-view SEM micrographs.[70] The profiles of the FeO_x microdisks were obtained using KLA Tencor P-15 profilometer performing a diagonal scan over the sample surface. Raman spectra were collected with an XploRA Raman system from HORIBA. The laser wavelength was 532 nm and the power modulation was reduced to 10% (1.2 mW). An acquisition time of 10 s and a 100× objective were used. X-ray photoemission electron spectroscopy (XPS) analyses were performed on continuous films (before and after voltage was applied) using a PHI 5500 Multitechnique System (Physical Electronics) with a monochromatic Al K_α (E = 1486.6 eV) source under ultrahigh vacuum. The XPS measurements were necessarily performed ex situ after having kept the sample inside an electrochemical cell (identical to that described above for the magnetic characterization) with the different values of voltage applied for 1 h. After voltage treatments, the samples were removed, cleaned in ethanol, and immediately placed in the XPS ultrahigh vacuum chamber. Data fitting was performed using the CasaXPS software.

Supporting Information

Supporting Information is available from the Wiley Online Library or from the author.

Acknowledgements

M.C. and A.N. contributed equally to this work. This work was supported by the European Research Council under the SPIN-PORICS 2014-Consolidator Grant, Agreement No. 648454 and the MAGIC-SWITCH 2019-Proof of Concept Grant, Agreement No. 875018. Partial financial support from the Generalitat de Catalunya (2017-SGR- 292 and 2018-LLAV-00032), the Spanish Government (MAT2017-86357-C3-1-R and associated FEDER), and the European Union's Horizon 2020 research and innovation program under the Marie Skłodowska-Curie Grant Agreement No. 665919 is also acknowledged. A.N. is thankful to the European Commission for the financial support through the H2020-MSCA-IF-2019 project (Agreement No. 892661—MAGNUS). G.R. acknowledges funding from RYC-2026-21412. The authors are also grateful to Dr. S. Auffret and Dr. V. Baltz from SPINTEC, Grenoble (France), for providing the metallized substrates used in this research. The authors would like to thank Dr. B. Bozzo from the Low Temperature and Magnetometry Service of the ICMAB (Spain) for his support in low-temperature magnetic measurements and the discussion of the results.

Conflict of Interest

The authors declare no conflict of interest.

Keywords

magnetoelectric effects, magneto-ionics, nanoporous iron oxide, phase transformations, voltage-driven switching of magnetism

Received: June 29, 2020
Revised: October 18, 2020
Published online: November 20, 2020

[1] A. Walther, C. Marcoux, B. Desloges, R. Grechishkin, D. Givord, N. M. Dempsey, *J. Magn. Magn. Mater.* **2009**, *321*, 590.
[2] K. Kim, J. Guo, X. Xu, D. Fan, *ACS Nano* **2015**, *9*, 548.
[3] N. Pamme, *Lab Chip* **2006**, *6*, 24.
[4] Y. Zhang, N. T. Nguyen, *Lab Chip* **2017**, *17*, 994.
[5] A. Hochstetter, *Micromachines* **2020**, *11*, 468.
[6] V. Zablotskii, A. Dejneka, Š. Kubinová, D. Le-Roy, F. Dumas-Bouchiat, D. Givord, N. M. Dempsey, E. Syková, *PLoS One* **2013**, *8*, e70416.
[7] H. T. Huang, Z. H. Wei, J. J. Liou, W. D. Zhao, X. Z. Xu, *Mater. Sci. Eng., C* **2019**, *104*, 109875.
[8] J. Pivetal, D. Royet, G. Ciuta, M. Frenea-Robin, N. Haddour, N. M. Dempsey, F. Dumas-Bouchiat, P. Simonet, *J. Magn. Magn. Mater.* **2015**, *380*, 72.
[9] T. R. Albrecht, H. Arora, V. Ayanoor-vitikkate, J.-M. Beaujour, D. Bedau, D. Berman, A. L. Bogdanov, Y. Chapuis, J. Cushen, E. Dobiaz, G. Doerk, H. Gao, M. Grobis, B. Gurney, W. Hanson, O. Hellwig, T. Hirano, P. Jubert, D. Kercher, J. Lille, Z. Liu, M. Mate, Y. Obukhov, K. C. Patel, K. Rubin, R. Ruiz, M. Schabes, L. Wan, D. Weller, T.-W. Wu, et al., *IEEE Trans. Magn.* **2015**, *51*, 1.
[10] R. F. Wang, C. Nisoli, R. S. Freitas, J. Li, W. McConville, B. J. Cooley, M. S. Lund, N. Samarth, C. Leighton, V. H. Crespi, P. Schiffer, *Nature* **2006**, *439*, 303.

[11] A. V. Chumak, A. A. Serga, B. Hillebrands, *J. Phys. D: Appl. Phys.* **2017**, *50*, 244001.
[12] E. Menéndez, H. Modarresi, C. Petermann, J. Nogués, N. Domingo, H. Liu, B. J. Kirby, A. S. Mohd, Z. Salhi, E. Babcock, S. Mattauch, C. Van Haesendonck, A. Vantomme, K. Temst, *Small* **2017**, *13*, 1603465.
[13] J. Sort, A. Concustell, E. Menéndez, S. Suriñach, K. V. Rao, S. C. Deevi, M. D. Baró, J. Nogués, *Adv. Mater.* **2006**, *18*, 1717.
[14] R. V. Mikhaylovskiy, E. Hendry, A. Secchi, J. H. Mentink, M. Eckstein, A. Wu, R. V. Pisarev, V. V. Kruglyak, M. I. Katsnelson, T. Rasing, A. V. Kimel, *Nat. Commun.* **2015**, *6*, 8190.
[15] A. V. Kimel, A. Kirilyuk, A. Tsvetkov, R. V. Pisarev, T. Rasing, *Nature* **2004**, *429*, 850.
[16] A. Kirilyuk, A. V. Kimel, T. Rasing, *Rep. Prog. Phys.* **2013**, *76*, 026501.
[17] Z. Diao, Z. Li, S. Wang, Y. Ding, A. Panchula, E. Chen, L. C. Wang, Y. Huai, *J. Phys.: Condens. Matter* **2007**, *19*, 165209.
[18] E. Albisetti, D. Petti, M. Pancaldi, M. Madami, S. Tacchi, J. Curtis, W. P. King, A. Papp, G. Csaba, W. Porod, P. Vavassori, E. Riedo, R. Bertacco, *Nat. Nanotechnol.* **2016**, *11*, 545.
[19] C. Navarro-Senent, A. Quintana, E. Menéndez, E. Pellicer, J. Sort, *APL Mater.* **2019**, *7*, 030701.
[20] C. Song, B. Cui, F. Li, X. Zhou, F. Pan, *Prog. Mater. Sci.* **2017**, *87*, 33.
[21] A. Molinari, H. Hahn, R. Kruk, *Adv. Mater.* **2019**, *31*, 1806662.
[22] J. M. Hu, C. W. Nan, *APL Mater.* **2019**, *7*, 080905.
[23] M. M. Waldrop, *Nature* **2016**, *530*, 144.
[24] S. Manipatruni, D. E. Nikonov, C. C. Lin, T. A. Gosavi, H. Liu, B. Prasad, Y. L. Huang, E. Bonturim, R. Ramesh, I. A. Young, *Nature* **2019**, *565*, 35.
[25] H. Cai, W. Kang, Y. Wang, L. A. De Barros Naviner, J. Yang, W. Zhao, *Appl. Sci.* **2017**, *7*, 929.
[26] R. Mishra, D. Kumar, H. Yang, *Phys. Rev. Appl.* **2019**, *11*, 54065.
[27] S. Robbennolt, A. Nicolenco, P. Mercier Fernandez, S. Auffret, V. Baltz, E. Pellicer, E. Menéndez, J. Sort, *ACS Appl. Mater. Interfaces* **2019**, *11*, 37338.
[28] U. Bauer, L. Yao, A. J. Tan, P. Agrawal, S. Emori, H. L. Tuller, S. Van Dijken, G. S. D. Beach, *Nat. Mater.* **2015**, *14*, 174.
[29] A. Quintana, E. Menéndez, M. O. Liedke, M. Butterling, A. Wagner, V. Sireus, P. Torruella, S. Estradé, F. Peiró, J. Dendooven, C. Detavernier, P. D. Murray, D. A. Gilbert, K. Liu, E. Pellicer, J. Nogues, J. Sort, *ACS Nano* **2018**, *12*, 10291.
[30] Q. Zhang, X. Luo, L. Wang, L. Zhang, B. Khalid, J. Gong, H. Wu, *Nano Lett.* **2016**, *16*, 583.
[31] A. J. Tan, M. Huang, C. O. Avci, F. Büttner, M. Mann, W. Hu, C. Mazzoli, S. Wilkins, H. L. Tuller, G. S. D. Beach, *Nat. Mater.* **2019**, *18*, 35.
[32] J. de Rojas, A. Quintana, A. Lopeandía, J. Salguero, B. Muñiz, F. Ibrahim, M. Chshiev, M. O. Liedke, M. Butterling, A. Wagner, V. Sireus, L. Abad, C. J. Jensen, K. Liu, J. Nogués, J. L. Costa-Krämer, E. Menendez, J. Sort, *Nat. Comm.* **2020**, https://doi.org/10.1038/s41467-020-19758-x.
[33] C. Bi, Y. Liu, T. Newhouse-Illige, M. Xu, M. Rosales, J. W. Freeland, O. Mryasov, S. Zhang, S. G. E. Te Velthuis, W. G. Wang, *Phys. Rev. Lett.* **2014**, *113*, 267202.
[34] N. Lu, P. Zhang, Q. Zhang, R. Qiao, Q. He, H. B. Li, Y. Wang, J. Guo, D. Zhang, Z. Duan, Z. Li, M. Wang, S. Yang, M. Yan, E. Arenholz, S. Zhou, W. Yang, L. Gu, C. W. Nan, J. Wu, Y. Tokura, P. Yu, *Nature* **2017**, *546*, 124.
[35] J. de Rojas, A. Quintana, A. Lopeandía, J. Salguero, J. L. Costa-Krämer, L. Abad, M. O. Liedke, M. Butterling, A. Wagner, L. Henderick, J. Dendooven, C. Detavernier, J. Sort, E. Menéndez, *Adv. Funct. Mater.* **2020**, *30*, 2003704.
[36] D. Larcher, C. Masquelier, D. Bonnin, Y. Chabre, V. Masson, J.-B. Leriche, J.-M. Tarascon, *J. Electrochem. Soc.* **2003**, *150*, A133.
[37] M. Nichterwitz, S. Neitsch, S. Röher, D. Wolf, K. Nielsch, K. Leistner, *J. Phys. D.: Appl. Phys.* **2020**, *53*, 084001.
[38] K. Duschek, A. Petr, J. Zehner, K. Nielsch, K. Leistner, *J. Mater. Chem. C* **2018**, *6*, 8411.
[39] L. Gloag, M. Mehdipour, D. Chen, R. D. Tilley, J. J. Gooding, *Adv. Mater.* **2019**, *31*, 1904385.
[40] M. Gich, I. Fina, A. Morelli, F. Sánchez, M. Alexe, J. Gàzquez, J. Fontcuberta, A. Roig, *Adv. Mater.* **2014**, *26*, 4645.
[41] E. Alphandéry, *Drug Discovery Today* **2020**, *25*, 141.
[42] L. Zhang, W. Hou, G. Dong, Z. Zhou, S. Zhao, Z. Hu, W. Ren, M. Chen, C. W. Nan, J. Ma, H. Zhou, W. Chen, Z. G. Ye, Z. De Jiang, M. Liu, *Mater. Horiz.* **2018**, *5*, 991.
[43] C. Navarro-Senent, A. Quintana, E. Isarain-Chávez, E. Weschke, P. Yu, M. Coll, E. Pellicer, E. Menéndez, J. Sort, *ACS Appl. Mater. Interfaces* **2020**, *12*, 14484.
[44] A. Quintana, J. Zhang, E. Isarain-Chávez, E. Menéndez, R. Cuadrado, R. Robles, M. D. Baró, M. Guerrero, S. Pané, B. J. Nelson, C. M. Müller, P. Ordejón, J. Nogués, E. Pellicer, J. Sort, *Adv. Funct. Mater.* **2017**, *27*, 1701904.
[45] C. Navarro-Senent, J. Fornell, E. Isarain-Chávez, A. Quintana, E. Menéndez, M. Foerster, L. Aballe, E. Weschke, J. Nogués, E. Pellicer, J. Sort, *ACS Appl. Mater. Interfaces* **2018**, *10*, 44897.
[46] L. A. Dubraja, C. Reitz, L. Velasco, R. Witte, R. Kruk, H. Hahn, T. Brezesinski, *ACS Appl. Nano Mater.* **2018**, *1*, 65.
[47] D. Chien, A. N. Buditama, L. T. Schelhas, H. Y. Kang, S. Robbennolt, J. P. Chang, S. H. Tolbert, *Appl. Phys. Lett.* **2016**, *109*, 112904.
[48] L. Klein, M. Aparicio, A. Jitianu, *Handbook of Sol-Gel Science and Technology*, Springer International Publishing, New York **2018**.
[49] A. A. Khaleel, *Chem. - Eur. J.* **2004**, *10*, 925.
[50] A. E. Danks, S. R. Hall, Z. Schnepp, *Mater. Horiz.* **2016**, *3*, 91.
[51] L. Durães, B. F. O. Costa, J. Vasques, J. Campos, A. Portugal, *Mater. Lett.* **2005**, *59*, 859.
[52] L. Durães, O. Oliveira, L. Benedini, B. F. O. Costa, A. Matos Beja, A. Portugal, *J. Phys. Chem. Solids* **2011**, *72*, 678.
[53] M. Hanesch, *Geophys. J. Int.* **2009**, *177*, 941.
[54] D. L. A. Faria, S. Venâncio Silva, M. T. de Oliveira, *J. Raman Spectrosc.* **1997**, *28*, 873.
[55] J. Xu, H. Yang, W. Fu, K. Du, Y. Sui, J. Chen, Y. Zeng, M. Li, G. Zou, *J. Magn. Magn. Mater.* **2007**, *309*, 307.
[56] D. Bersani, P. P. Lottici, A. Montenero, *J. Raman Spectrosc.* **1999**, *30*, 355.
[57] M. Estrader, A. López-Ortega, I. V. Golosovsky, S. Estradé, A. G. Roca, G. Salazar-Alvarez, L. López-Conesa, D. Tobia, E. Winkler, J. D. Ardisson, W. A. A. Macedo, A. Morphis, M. Vasilakaki, K. N. Trohidou, A. Gukasov, I. Mirebeau, O. L. Makarova, R. D. Zysler, F. Peiró, M. D. Baró, L. Bergström, J. Nogués, *Nanoscale* **2015**, *7*, 3002.
[58] F. J. Morin, *Phys. Rev.* **1950**, *78*, 819.
[59] Ö. Özdemir, D. J. Dunlop, T. S. Berquó, *Geochem., Geophys., Geosyst.* **2008**, *9*, n/a.
[60] P. C. J. Graat, M. A. J. Somers, *Appl. Surf. Sci.* **1996**, *100-101*, 36.
[61] T. Yamashita, P. Hayes, *Appl. Surf. Sci.* **2008**, *254*, 2441.
[62] W. S. M. Werner, *Surf. Interface Anal.* **2001**, *31*, 141.
[63] M. P. Seah, W. A. Dench, *Surf. Interface Anal.* **1979**, *1*, 2.
[64] M. E. Fleet, *Acta Crystallogr., Sect. B: Struct. Sci., Cryst. Eng. Mater.* **1981**, *37*, 917.
[65] J. Zhang, W. Liu, M. Zhang, X. Zhang, W. Niu, M. Gao, X. Wang, J. Du, R. Zhang, Y. Xu, *J. Magn. Magn. Mater.* **2017**, *432*, 472.
[66] J. Grangle, G. M. Goodman, *Proc. R. Soc. London, Ser. A* **1971**, *321*, 477.
[67] M. P. Morales, S. Veintemillas-Verdaguer, M. I. Montero, C. J. Serna, A. Roig, L. I. Casas, B. Martínez, F. Sandiumenge, *Chem. Mater.* **1999**, *11*, 3058.
[68] J. Read, K. Mutolo, M. Ervin, W. Behl, J. Wolfenstine, A. Driedger, D. Foster, *J. Electrochem. Soc.* **2003**, *150*, A1351.
[69] O. V. Tripachev, E. A. Maleeva, M. R. Tarasevich, *Russ. J. Electrochem.* **2015**, *51*, 103.
[70] C. A. Schneider, W. S. Rasband, K. W. Eliceiri, *Nat. Methods* **2012**, *9*, 671.